Effects of Proton Irradiation on the Mechanical and Physical Properties of Carbon Nanotube Based Composites

Anthony J. Nelson

Thesis submitted to the faculty of the Virginia Polytechnic Institute and State University in partial fulfillment of the requirements for the degree of

Master of Science

In

Engineering Mechanics

Marwan Al-Haik, Chair

Mark Pierson

Scott Case

December 4, 2013

Blacksburg, VA

Keywords: Carbon Nanotubes, Proton Radiation, Radiation Shielding, Nanocomposites

Effects of Proton Irradiation on the Mechanical and Physical Properties of Carbon Nanotube Based Composites

Anthony J. Nelson

Abstract

Exposure to proton radiation is a major concern for space travel as the space environment is filled with energetic protons from solar particle events (SPEs), galactic cosmic radiation (GCR), and trapped radiation belts. In this study, the effects of proton irradiation on carbon nanotube (CNT)-epoxy composites are investigated for potential applications in radiation shielding for spacecraft. CNT-epoxy composites were prepared using multiwall and single wall CNTs and exposed to proton beams of energies ranging from 6 MeV to 12 MeV. The nanocomposites' shielding capabilities against the different energetic proton beams were measured by tracking the beam's energy before and after penetrating the samples. The microstructures of the samples were characterized using scanning electron microscopy (FESEM). The effect of proton irradiation on the electrical resistivity was measured using a high resolution multimeter. Finally the influence of the irradiation on the mechanical properties, such as the elastic modulus and hardness, was probed using instrumented nanoindentation tests.

The proton stopping power of the epoxy was shown to be unchanged by the addition of CNTs, which is a promising result since this will allow using shields with more carbon content than hydrogen; adding structural functionality to the shielding material. While the hardness of the samples was shown to be increased by addition of CNTs, the surface of the samples proved to be too rough for nanoindentation to yield more detailed results. This was due to the use of a

diamond saw in cutting the samples to size. The addition of CNTs was shown to reduce the volume electrical resistivity of the neat epoxy by almost five orders of magnitude and the irradiation further reduced it by a factor of 2-16.

Table of Contents

Table of Figures

List of Tables

Chapter 1: Introduction

1.1 Cosmic Radiation

Cosmic radiation is one of the most crucial challenges for interplanetary space travel, specifically for manned missions outside Low Earth Orbit (LEO). This radiation poses a significant health risk to astronauts and can damage sensitive equipment. In fact, it has been identified as one of the primary health concerns to crews on long term missions [1]. Protecting crews from harmful radiation is a complicated and important challenge for extended manned space flight.

The general radiation environment in space from all sources is referred to as *cosmic radiation*. Cosmic radiation is comprised of various charged particles, including protons, electrons, and ions of heavy elements with a range of energies and fluences depending on many factors such as spacecraft trajectory, time of the solar cycle, and rare solar events [2]. The space radiation environment stems from three primary sources: (1) galactic cosmic radiation (GCR), (2) solar particle events (SPEs), and (3) trapped radiation belts. Sometimes a fourth source, albedo neutrons and protons, is also considered. These are secondary particles that result from the interactions between GCR and the atmosphere of Earth. However, they are of low energy and are not usually considered a significant source of radiation [3].

1.1.1 Galactic Cosmic Radiation

Galactic cosmic radiation (GCR) consists of charged particles originating from beyond the solar system. They are of somewhat mysterious origin, but there is evidence that a significant portion of GCR comes from supernovae of massive stars [4]. The distribution of GCR is believed to be

isotropic throughout interstellar space with energies reaching as high as 10^{12} MeV. The spectrum is peaked around 1.0 GeV in the solar system [3] and the maximum particle fluence rate has been estimated to be around 4 particles/(cm^2-s-sr) at solar minimum [5]. The GCR spectrum of Earth's orbit is made up of approximately 83% protons, 13% alpha particles, 3% electrons, and 1% nuclei with Z greater than 2 [6]. The composition of GCR as measured on Earth and in the solar system is shown in Figure 1.

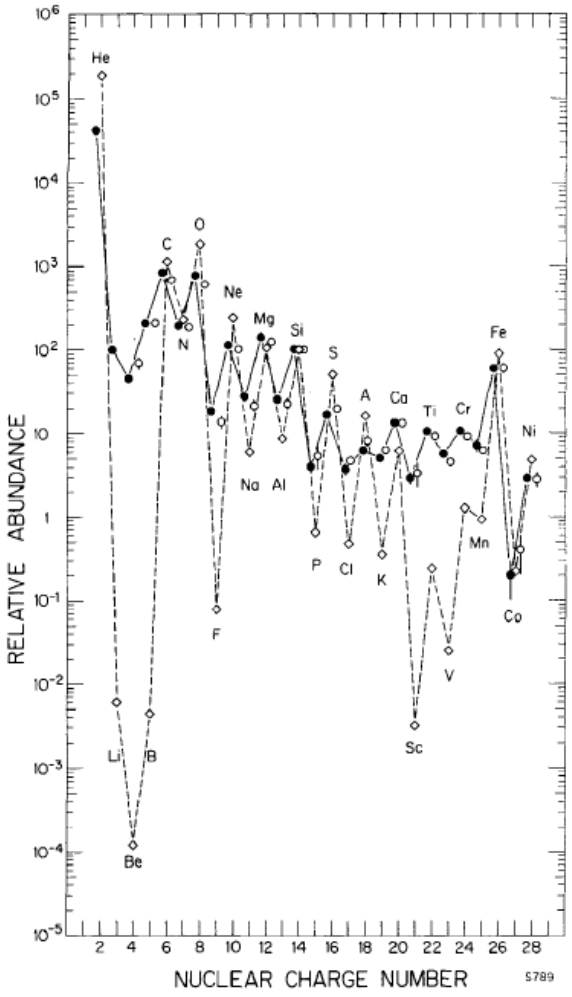

Figure 1: Cosmic radiation elemental abundance relative to Si for He through Ni Measurements taken at Earth (circles) and in the solar system (diamonds). Solid circles represent low energy data from 70-280 MeV n^{-1}. Open circles represent high energy data from 1000-2000 MeV n^{-1}. [7] Image used under fair use

Spacecraft in LEO are protected to some degree by the Earth's magnetic field, but for high inclination orbits GCR is the dominant source of radiation exposure. For example, GCR accounts for roughly half of the radiation exposure of the International Space Station [3]. GCR is omnipresent in free space, but the flux of the lower energy components in the solar system is inversely proportional to the solar cycle [7].

Fragments are reactive products of the GCR which have undergone nuclear interaction. They are also a concern, but they make up a small portion of the overall radiation [8]. A 1.0 GeV proton can penetrate approximately 400 g/cm^2 of Al [6]. Since this amount of shielding is obviously impractical, new methods of shielding GCR must be explored.

1.1.2 Solar Particle Events

A solar particle event (SPE) occurs when particles emitted by the sun are accelerated by a solar flare or the shock wave associated with a coronal mass ejection (CME). SPEs are made up of protons, helium, and heavier ions [2]. SPEs have been described as falling into two different categories: ordinary and anomalously large events [9]. Anomalously large events occur rarely (usually less than five per 11 year solar cycle) but when they do occur their fluence can exceed 10^{10} protons/cm^2 and may often have energies above 10 MeV [2]. Figure 2 shows the energy spectra of selected SPEs.

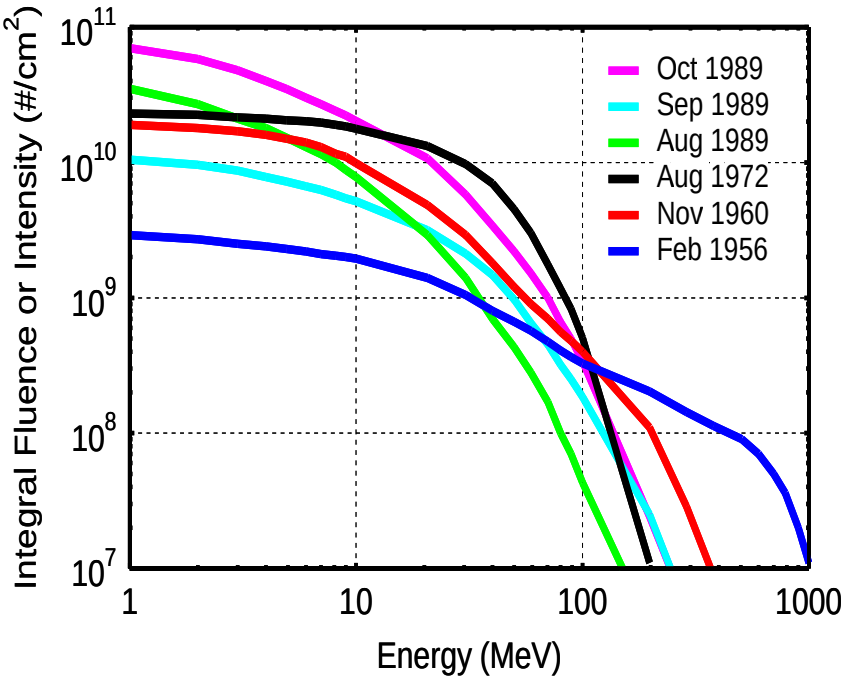

Figure 2: Spectra of large solar events from 1956 to 1990 [10]. Image used under fair use

Between 1955 and 1989 more than 200 SPEs were recorded with flux over 10 particles/(cm^2-s-sr) and energy above 10 MeV, and at least 15% of these events had energies greater than 450 MeV [6]. One probabilistic approach [11] predicts that the fluence of ordinary SPEs over a 90 day mission is only around 3% as large as the fluence of a single anomalously large SPE. For short missions, anomalously large SPEs have been considered an unlikely event, but for a mission lasting 3 years, there is a 25%-50% chance of occurrence, and precautions must be taken [12].

1.1.3 Trapped Radiation Belts

There are two types of radiation trapped in Earth's magnetic field: electron belts and proton belts. Electrons are trapped in two regions around the Earth. The inner zone extends to about

2.8 Earth radii at the equator and the outer zone lies between 2.8 and 12 Earth radii at the equator as shown in Figure 3 [2].

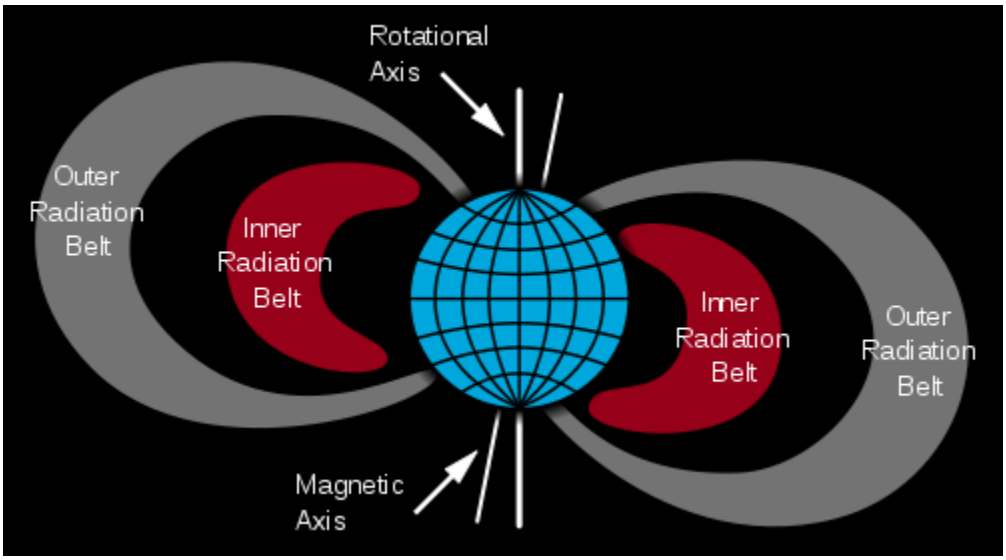

Figure 3: Trapped radiation belts [13]. Image used under fair use

The electron intensities in the outer zone are an order of magnitude higher than those in the inner belt and their energies are also much higher [5]. For geosynchronous orbit at an altitude of around 36,000 km, these electrons dominate the radiation exposure [14].

Trapped protons are the most important source of radiation for LEO missions with an altitude around 450 km. The trapped particles spiral closer to the Earth over the South Atlantic Ocean creating a region of high radiation flux called the South Atlantic Anomaly [14]. A large fraction of the radiation exposure of a LEO mission comes from a 15-30 minute period while it passes through this anomaly.

1.2 Radiation Shielding

Radiation shielding is an important challenge facing both manned and unmanned space flights. In manned missions, protecting astronauts from carcinogenic damage caused by cosmic radiation is a major priority and in unmanned space flights sensitive equipment must be protected from radiation that can damage it or cause it to malfunction.

The danger of high-energy particles to astronauts is directly related to the amount of energy deposition in body tissue as well as the composition and ionizing effect of the transmitted radiation. Upon nuclear collisions, both the incident GCR ions as well as the target nuclei can fragment to smaller charges, thus reducing their effective ionization damage which is related to the square of their atomic charge.

For example, the incident GCR will fragment silicon into carbon and helium-4 particles that are of lower relative biological effectiveness (RBE) and thus less hazardous. The relative biological effectiveness (RBE) is defined as the ratio the doses required by two ionizing radiations, with identical amount of absorbed energy, to cause the same level of effect (mainly damage) on biological organs. Thus, the RBE depends on the dose and the biological endpoint [15].

If the shield material is iron, incident GCR will fragment iron into chromium or silicon particles of higher RBE, which are thus more hazardous [16]. Hence, the primary consideration in mitigating the adverse biological effects of space radiation is not necessarily to prevent ions from penetrating the interior environment, which is difficult and impractical to do, but rather to reduce

the effective RBE of such collisions via spallation and fragmentation and with minimal production of secondary radiation, including high energy neutrons and alpha particles.

In 1989, the National Council on Radiation Protection (NCRP) [2] estimated that, for LEO missions, 2.5 g/cm^2 of aluminum would be sufficient to meet the 500 mSv limit for the exposure of blood forming organs. Applying this standard to the Mars Reference Mission, it is estimated that an aluminum shield thickness above 50 g/cm^2 would be required, which is impractical [16]. Since then, the limit has been reduced to 200 mSv, making this requirement even more challenging. The fact that the high energy particles in space can fragment in the shield, further exposing the astronaut, complicates matters [17]. For the low energy (50-70 MeV) radiation in space, the walls of the spacecraft provide total protection, but during some intense solar events the dose released in a few hours can exceed the limits for astronaut safety and can lead to acute effects including lethal radiation syndromes [18].

Several other materials have been identified as potentially promising for shielding purposes. These are liquid hydrogen, hydrogenated nanofibers, liquid methane, LiH, polyethylene, polysulfone, and polyetherimide (in order of improving shield performance) [19]. The critical issue is knowledge of the biological effect of the specific particle mixture behind the shield material and the modification of that mixture by the proper selection of material.

The effectiveness of a potential shielding material is measured by its ability to attenuate the radiation intensity as it traverses the material. In case of GCR and SPEs, however, the production of secondary particles is a key differentiator. In addition to ionization losses, the traversing GCR

ions and SPEs produce, through nuclear collisions, secondary light fragments and neutrons that can contribute significantly to the exposure dose. In fact, for some materials (aluminum and heavier) at certain thicknesses the contribution of the secondary particles to the total dose-equivalent actually exceeds that of the primary particles [20]. The ability to reduce the dose-equivalent (as opposed to the dose itself) per unit length (or area density) of the material determines its *shielding effectiveness*. In this regard, light materials, e.g., polymeric ones, are, in general, more effective than heavier ones such as aluminum [10, 21]. Figure 4 contrasts the shielding effectiveness of a few select materials [10]. In this figure, the mission exposure limit for Mars is extrapolated from that for a low-earth orbit (LEO). Points M1-M4 give the corresponding depth in each material that intersects this hypothetical limit in units of the material's area density. In Figure 4, LH_2 refers to liquid hydrogen and PE to polyethylene and the assumed radiation environment is a hypothetical worst-case scenario of solar-minimum GCR conditions superposed on a September 1989-class solar particle event (SPE).

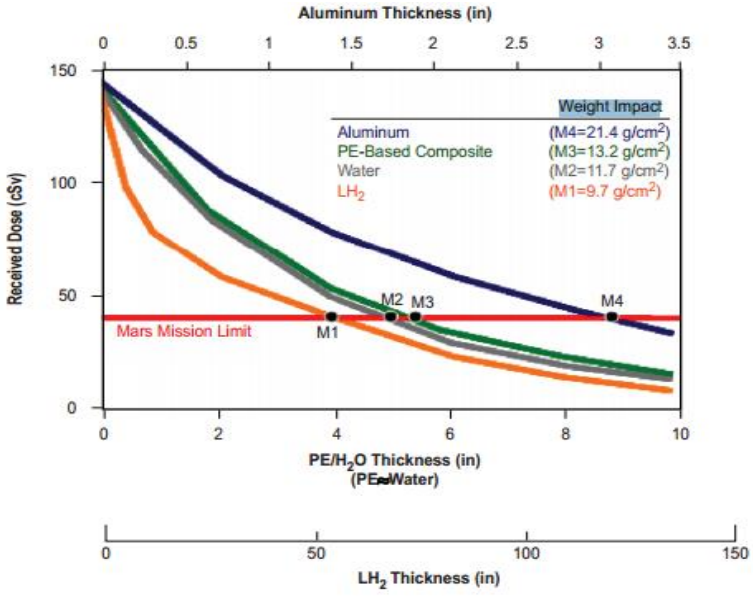

Figure 4: Calculated dose-equivalent as a function of depth in various potential shielding materials [10]. Image used under fair use

The general approach in the past has been to simply add more aluminum to increase shielding, but for manned missions of extended duration this is simply not an option. Aluminum has the advantage of being a good structural material, but it is relatively heavy, which is a major concern for space flight, as each extra kilogram of mass increases the mission cost by approximately $36,000 (for geosynchronous orbit as of 2002) [22].

Materials with the most electrons per unit mass, the least mean excitation energy, and the least tight binding corrections make the best energy absorbers [19]. Studies performed at NASA Langley Research Center (LaRC) have shown that with a minimal cascading effect (secondary production), liquid hydrogen, while structurally of no significance, is the best shielding material for cosmic particulate radiation (Figure 4). Therefore, a material with a high hydrogen number density and that is structurally able to withstand the hazards of space would be an ideal shielding candidate for space applications. Polymers have high hydrogen content, and in a crystalline state (e.g., polyethylene) have a very predictable uniform concentration throughout. They also comprise carbon and oxygen, which are lightweight elements with negligible cascading properties. Amorphous polymers (e.g., epoxy) have far fewer reaction channels and nuclear secondary interactions, and therefore lower channeling radiation hazards.

Polyethylene is a light material that provides good protection from energetic protons. It has been concluded that polyethylene is the best "standard or non-novel" material, except for pure hydrogen, for radiation protection because of its high hydrogen content and the fact that it preferentially fragments into alphas rather than neutrons [23].

Polymeric substances, however, exhibit a wide variety of radiation effects. These include the formation of new chemical bonds after irradiation usually resulting in irreversible effects, which are manifested as changes in appearance, chemical and physical states, and mechanical, electrical, and thermal properties. However, not all properties of a polymer are affected by radiation exposure to the same degree. The radiation stability of a polymer depends upon its chemical structure, but since radiation-induced excitation is not coupled to the entire chemical system, it is often localized at a specific bond. The addition of energy-absorbing aromatic rings to the chemical structure significantly increases the radiation stability of some polymers by aiding the redistribution of the excitation energy throughout the material. Conversely, those polymers with highly aliphatic structures (e.g., ethers and alcohols) are the least resistant to radiation [24].

One might suspect that heavy metals such as lead would be useful for shielding cosmic radiation, but it has been shown that 20 g/cm^2 of lead provides no reduction at all in tissue doses from GCR [19, 25, 26]. In fact, that same amount of hydrogen or oxygen (or materials containing these elements, such as water and polyethylene) provides significantly better shielding [19].

Evidence suggests that carbon is the second most efficient shielding element for GCR after hydrogen [23] . Carbon nano-allotropes, including fullerenes, graphene, and carbon nanotubes, possess significantly better physical, electrical, and thermal properties than polymers. Additionally, carbon nanotubes (CNTs) have shown some capacity for hydrogen storage, which would further increase their efficiency. CNTs have shown hydrogen storage in the range of 5-67

wt%, which is higher than the hydrogen content of polyethylene [27-30]. Carbon nanostructures show promise as shielding materials, especially in the form of composites with polymers.

Another option for shielding cosmic radiation is active shielding, where a magnetic field is generated around the spacecraft to divert charged particles, much like the protective magnetic field of the Earth. Active shields fall into 4 categories: electrostatic shields, plasma shields, confined magnetic shields, and un-confined magnetic shields [23]. These types of shields have the advantage of powerful blocking of charged particles, but they also have several drawbacks. They typically require large energy input which either necessitates massive generators or increased solar cells. Additionally some missions, such as the Radiation Belt Storm Probes (RBSP) mission, require electromagnetic cleanliness. The RBSP is required to have a residual magnetic field of less than 5 nT [31], which essentially removes active shielding as an option.

1.3 Carbon Nanotubes

In 1991, carbon nanotubes (CNTs), cylindrical allotropes of carbon, were coincidently discovered using carbon arc discharge synthesis [32]. This new form of carbon exhibits excellent physical, electrical, and thermal properties and has been the subject of a growing body of research. Schematically a single sheet of graphene (a sheet of hexagonally patterned carbon, 1 atom thick) rolled into a cylinder, CNTs have diameters as small as 0.5 nm and aspect ratios as high as 132,000,000:1 [33]. There are two classes of CNTs: single walled nanotubes (SWCNTs), which are composed of a single cylinder of graphene, and multiwall nanotubes (MWCNTs), which include several concentric SWCNTs stacked within each other. Figure 5 shows a schematic of the two types of CNTs.

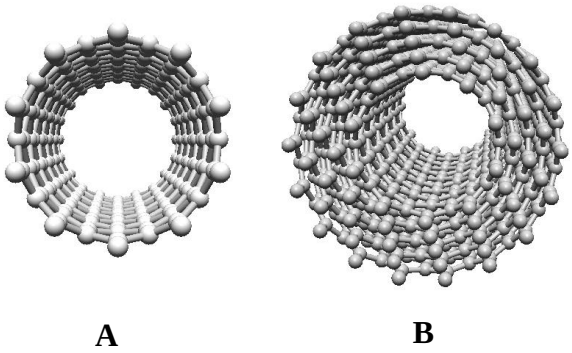

Figure 5: (A) Single walled nanotube and (B) multiwall carbon nanotube.

There are three classes of CNT patterns: armchair, zigzag, and chiral. Figure 6 shows a schematic of the three patterns of CNTs. This pattern plays an especially important role in determining the electrical properties of CNTs.

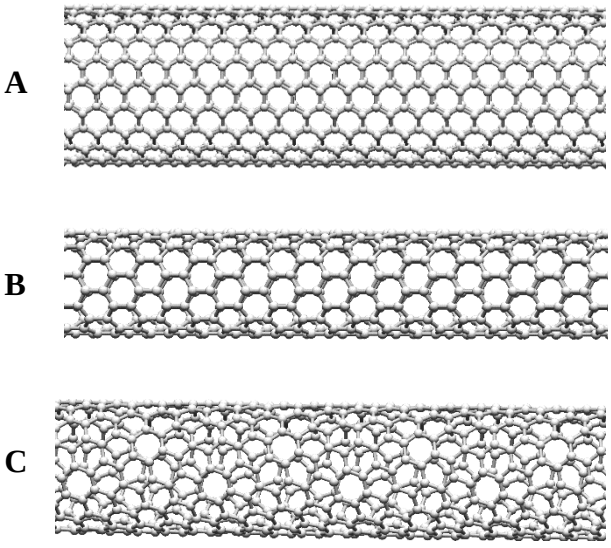

Figure 6: Schematic of (A) armchair, (B) zigzag, and (C) chiral SWCNTs.

While the procedure for producing CNTs is very different from that of graphene, one can think of CNTs as being cut from a sheet of graphene then rolled into a cylinder. The angle of the cut, called the chiral angle, determines the pattern of the nanotube as shown in Figure 7.

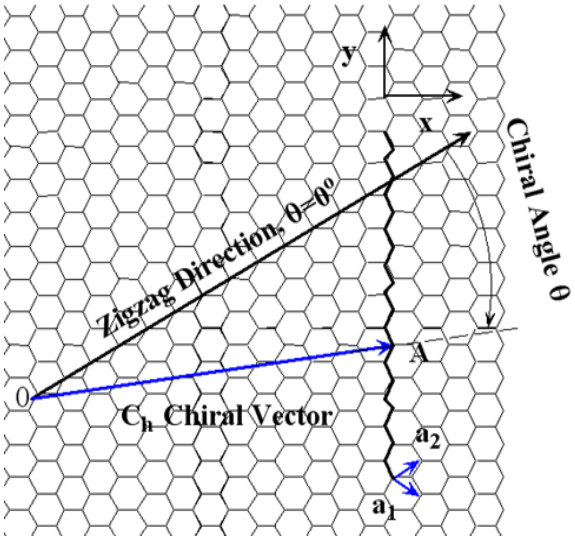

Figure 7: Chiral angles

The chiral vector can be described by

$$\vec{C}_h = n\vec{a}_1 + m\vec{a}_2 \tag{1}$$

where the integers (m, n) are referred to as the chiral indices; the number of steps along the zigzag carbon bonds of the hexagonal lattice in their respective directions [34]. A chiral angle of 0^o, or equivalently a rollup vector of $(n, 0)$, results in a zigzag pattern. A chiral angle of 30^o and rollup vector of (n, n) results in an armchair pattern, while all other angles result in what are called chiral patterns [34].

1.3.1 Mechanical Properties

Carbon nanotubes have excellent mechanical properties that vary depending on the tube dimensions, number of defects, whether they are SWCNTs or MWCNTs, and the chirality. Many studies have been conducted to measure the mechanical properties of CNTs but, because of the challenges associated with the size of CNTs, there is wide scatter among the data. Young's modulus is generally reported to be around 1.0 TPa, and the single tube strength has been reported from 13 to 150 GPa with most estimates being around 45 GPa [34-45]. Poisson's ratio of a CNT has been estimated to be 0.16 [46].

Because CNTs are so small, it is difficult to directly measure their mechanical properties in conventional ways but many different strategies have been used to make reliable estimates. The first measurement was made by observing, in a TEM, the amplitude of thermal vibrations of cantilevered CNTs [35]. This resulted in an average Young's modulus of 1.8 TPa, but with significantly scattered data. Since then, the same method was improved upon, getting an average Young's modulus of 1.25 TPa with much less scatter [37].

Another group applied a bending force to cantilevered CNTs with an AFM and measured the resulting deflection. This technique resulted in an average Young's modulus of 1.28 TPa in low defect MWCNTs [38] and 0.81 TPa in high defect SWCNT [39]. The strength can also be measured in this way, but failure is due to buckling rather than breaking of atomic bonds. Strength was estimated at 28.5 GPa using this method but it should be noted that this value is

likely lower than the tensile strength [38]. Another group measured the strain on the outer wall of a bent nanotube to calculate a strength of 150 GPa [42].

Yu et al. directly performed tensile tests on MWCNTs in a SEM and measured Young's moduli from 0.27 to 0.95 TPa and strengths ranging from 11 to 63 GPa [40]. Another group immersed CNTs in a matrix material in order to subject it to tensile loads [43]. They found an estimated strength of 45 GPa. A SWCNT rope was exposed to a sideways pull resulting in a calculated strength of at least 45 GPa [44]. With a combination of tensile and bending tests, another group estimated the strength to be 150 GPa [45].

Carbon nanotubes have also shown extraordinary resilience, enduring significant deformations and changes to their shape without permanent atomic rearrangements [41]. They have been found to develop kinks or flatten into ribbons, and subsequently return to their original shape without damage.

1.3.2 Electrical Properties

The electrical properties of CNTs may be even more exciting and revolutionary than their mechanical properties. They may behave as metals or semiconductors, depending on their chirality. As metals they demonstrate high conductivity and can act as molecular wires. As semiconductors they show great promise for a wide range of applications due to the ease with which their electrical properties can be tuned.

Chirality plays a much more important role in the electrical properties of CNTs than it does in their mechanical properties. It is the primary indicator of whether a CNT will behave like a conductor or a semiconductor. Practically all armchair (n, n) SWCNTs are metallic while zigzag $(n, 0)$ and chiral (n, m) SWCNTs are only metallic if $n - m$ is a multiple of 3 [47]. Otherwise, they are semiconductors with band gap dependent primarily on the diameter [48].

Metallic SWCNTs have a theoretical intrinsic two-terminal resistance of only 6.5 kΩ [41], however it is difficult to measure because the resistance is typically dominated by contact resistance. By evaporating metal on top of the nanotubes, Soh et al. measured a two-terminal resistance as low as 10 kΩ [49].

Many of the unique electrical properties of semiconducting CNTs arise due to the small length scale because quantum effects dominate, but graphite itself also has unique electrical properties. Graphite is one of only a few semimetals, which have only a very small overlap between the bottom of the conduction band and the top of the valence band. Semiconducting CNTs combine the unique semimetallic properties of graphite with the quantum effects of nanotubes to create very interesting and unusual properties [50]. The band gaps of CNTs can be made as low as zero, as in the case of metallic CNTs, or as high as silicon, and almost anywhere in between by adjusting their dimensions, which makes them possibly the most tunable semiconductor in existence [50]. Because of their unique electrical properties, CNTs are being explored for applications ranging from light bulbs and flat panel displays to nanocircuits and microcomputing.

1.4 Effects of Radiation

Radiation tends to degrade the mechanical properties of most materials, including CNTs and polymers. It also changes other characteristics of materials such as their electrical, thermal, and optical properties.

1.4.1 Effect of Radiation on CNTs

The effects of radiation on CNTs were first studied with the goal of using radiation to impose beneficial changes to the structure of the CNTs, but there has been some recent focus on CNTs for their potential use in radiation environments.

Electron radiation has been a major focus of studies so far, in part because several microscopy techniques use electron beams that cause damage to CNTs. It has been shown that high energy electron beams can cause vacancies and displacements of atoms to interstitial positions [51]. Point defects of this kind modify the electronic properties of CNTs near the Fermi level, making this technique potentially useful for tuning CNTs for electronic applications [52]. These vacancies were observed to cause coalescence of CNTs under electron irradiation at high temperatures [53], which prompted further investigation into methods of using irradiation to change the structure of CNTs in a useful manner.

Ion radiation was also shown to result in useful manipulations of CNT structure. Krasheninnikov et al. showed that ion bombardment should result in a similar welding of nanotubes [54]. In another study they also reported severe damage to nanotubes as a result of ion bombardment [55]. The most prolific effects of ion bombardment on CNTs are vacancies on the

walls of the nanotubes [56]. Wei et al. found that 50.0 keV doses with a fluence of about 10^{13} ions/cm^2 did not cause any significant damage to the outer walls of MWCNTs but caused the inner walls to organize into tiny ordered nanocompartments [57]. They found that increasing the fluence to 10^{14} ions/cm^2 resulted in destruction of the nanocompartments, while at 10^{15} ions/cm^2 the MWCNTs degenerated into amorphous rods [57]. Ions of energy less than 1.0 keV were found to lose about 0.3 keV of their kinetic energy in a single collision with a CNT shell [56].

Proton irradiation of CNTs is a particularly under-investigated field. However, there are some good studies into the effects of proton beams on CNTs. Ishaq et al. reported that, after irradiation with 70.0 keV protons at a fluence of 1018 p/cm^2, the nanotubes became completely amorphous [58]. CNTs in a poly(3-octylthiophene) matrix were subjected to 2.0 MeV proton irradiation at fluences from 5×10^{10} to 5.6×10^{15} p/cm^2 by Neupane et al [59]. Subsequent broadening of the interband transition spectra and reduction of the radial breathing mode intensity as observed by Raman scattering showed some radiation related degradation.

The proton stopping power of MWCNTs were calculated and found to be somewhat less than that of amorphous carbon, as shown in Figure 8. Two methods were used to calculate the proton stopping power of MWCNTs, and the actual value is thought to be between the two [60].

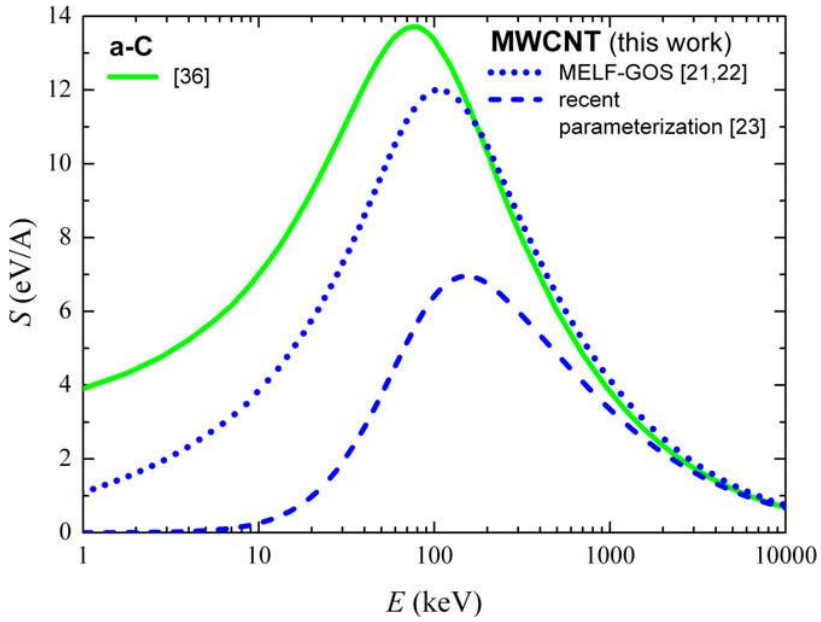

Figure 8: Calculated proton stopping power of amorphous carbon (green), and MWCNTs (blue dotted lines)[60]. Image used under fair use

1.4.2 Effects of Radiation on Polymers

Radiation has a variety of effects on polymers including cross-linking, chain scission, gas evolution, formation of double bonds, and formation of end groups, all of which contribute to changes in the physical, electrical, and optical properties [61-66]. In flexible polymers, cross-linking as a result of ionization tends to increase the Young's modulus while reducing the strain to failure [62]. Chain scission decreases the elastic modulus, yield stress for plastic flow, hardness, and elasticity while increasing elongation [62]. Chain scission is also sometimes responsible for embrittlement and gas evolution.

Sasuga et al. [67], measured the effect of 8 MeV protons, 30 MeV He^{2+}, 80 MeV C^{4+}, and N^{4+} on the tensile properties of eight aliphatic polymers and four aromatic polymers. In all cases they found degradation of the tensile strength and ultimate elongation. They found practically no

difference in the dose dependence between electron and proton irradiation in the aliphatic polymers, but the decrements in the tensile strength and ultimate elongation as a function of proton dose were less than those for electron irradiation in the aromatic polymers.

Parada et al. [68] bombarded the polymers tetrafluoroethylene-per-fluoromethoxyethylene (PFA) and tetrafluoroethylene-hexa-fluoropropylene (FEP) with 1 MeV protons at constant current and fluence from 1×10^{11} to 1×10^{16} ions/cm^2. Using a residual gas analyzer they found emission of CF_3 in both polymers. Using optical absorption photospectrometry (OAP), micro-Raman, and Fourier transform infrared (FTIR), they demonstrated the formation of carbon double bonds. Mishra et al. [64] found an increase in the conductivity of Polypropylene (PP) when irradiated with 2 MeV electron and 62 MeV proton beams. It is believed that the primary cause of the increase in conductivity is the increase in conjugated double bonds which promote the motion of charge carriers along the polymeric chains. Little et al. [66] found that irradiating polymers with electrons caused the breaking of both ionic and covalent bonds, as well as the formation of carboxyl end-groups.

Kudoh et al. [63] measured the flexural strength at break of poly(methyl methacrylate) (PMMA) and glass fiber reinforced plastic (GFRP) before and after irradiation with protons of energies 30 and 45 MeV. They also measured the effect of irradiation with Co^{60} gamma rays and found that both forms of irradiation degrade the flexural strength of PMMA and GFRP by essentially the same amount. Al-Haik et al. [62] showed that proton radiation damage could be mitigated by magnetically orienting epoxy. However, magnetically orienting the epoxy also reduced the

stopping power, indicating that there is a trade-off between stopping power and mechanical properties.

Gao et al. [69] irradiated AG-80 epoxy resin and unidirectional M40J/AG-80 composites with 150 keV protons and measured changes in the bend strength, bend modulus, interlayer shear strength, and mass loss. They showed that the cross-linking density increased with the fluence in the surface layer when the proton fluence was lower than 5.5×10^{15} p/cm^2, which increased the modulus and bend strength of the composite. When they increased the fluence beyond $5.5x10^{15}$ p/cm^2, they found that the cross-linking density, bend strength, and bend modulus decreased. The interlayer shear strength showed a similar trend. With increasing proton fluence, the mass loss ratios for both the AG-80 epoxy resin and the M40J/AG-80 composites increased first and then leveled off.

1.5 Thesis Outline

The objective of this thesis was to probe the effects of proton irradiation on CNT-epoxy composites. Three types of samples were fabricated: neat epoxy samples, SWCNT-epoxy composites, and MWCNT-epoxy composites. The effects of irradiation on the electrical and mechanical properties of neat epoxy samples and composite samples containing SWCNTs and MWCNTs were measured.

CNTs were purified using an acid treatment, then carefully dispersed within the epoxy matrix before being cured and cut to the desired dimensions. They were sent to Florida State University

where they were irradiated with protons in their Van de Graaff accelerator. The facilities at FSU were also used to measure the proton stopping power of the samples.

After irradiation, a series of tests were performed on both the radiated and the non-radiated samples to determine the effect of irradiation. The resistivity was measured using a high resolution multimeter utilizing an alternating current technique to improve repeatability. Finally the influence of the irradiation on the mechanical properties, such as modulus and hardness, was probed with instrumented nanoindentation tests.

Chapter 2: Experimental Setup and Procedure

2.1 Materials

The matrix material used in this study was Aeropoxy PR2032 resin, which is produced by PTM&W industries, Inc. PR2032 is a medium viscosity, unfilled, light amber laminating resin that is designed for use in fabricating composite parts and other demanding structural applications. This resin laminates very easily, and wets out fiberglass, carbon, and aramid fibers readily. When mixed with PH3660 hardener, it cures at room temperature in 24 hours. PR2032 contains diphenylolpropane (bisphenol A), a multifunctional acrylate, and some acrylic monomers. The hardener component, Aeropoxy PH3660, is a modified amine mixture. These materials do not contain any metallic compounds. This epoxy system was used to manufacture all of the samples used in this study. The properties of this epoxy system as provided by the vendor can be found in Table 1.

The carbon nanotubes used in this investigation were high purity MWCNTs and SWCNTs purchased from Cheap Tubes Inc. The MWCNTs had a purity of at least 95 wt%, an outer diameter less than 8.0 nm, and a length between 10.0 and 30.0 μm. The SWCNTs had a purity of at least 90 wt%, an outer diameter between 1 and 2 nm, and a length between 5 and 30 μm. The properties of these CNTs are provided in Table 1.

Table 1: Material Properties

Material	PR2032 Epoxy	MWCNT	SWCNT
Elastic Modulus (GPa)	2.88	~1000	~1000
Tensile Strength (GPa)	0.068	13-150	13-150
Electrical Conductivity (S/cm)	10^{-6}	>100	>100
Bulk Density (g/cm^3)	1.13	0.27	0.14
True Density (g/cm^3)	1.13	~2.1	~2.1

2.2 Composite Sample Preparation

In order to remove metal contaminants, the carbon nanotubes were treated for two hours with a 1:1 mixture of nitric acid and sulfuric acid with a molarity of 6.0 M. The mixture was then repeatedly washed with deionized water and centrifuged until reaching a pH of 7.0. The nanotubes were then dried in a furnace at 70^{o} C. The effect of acid treatment is shown in Figure 9, where the impurities (the dark spots) seen in the untreated sample are far less visible upon acid treatment.

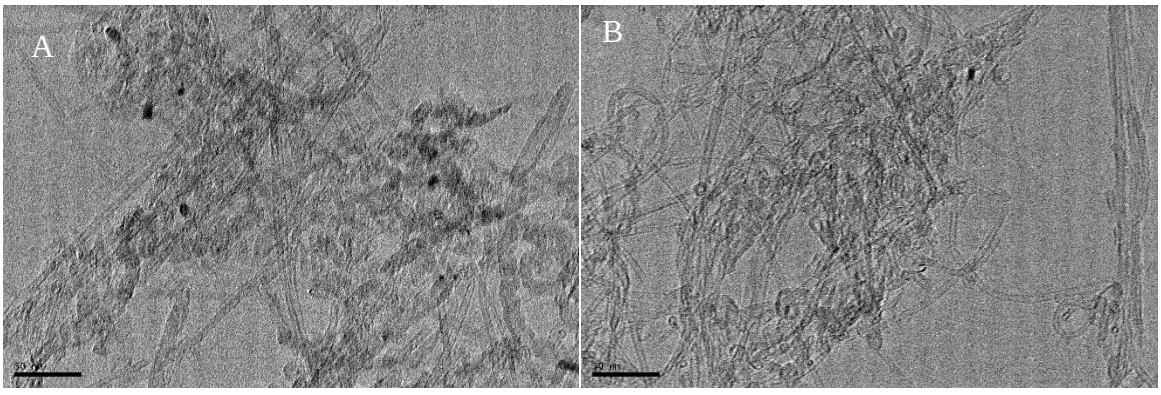

Figure 9: TEM micrographs of MWCNTs (A) before and (B) after acid treatment.

Carbon nanotubes tend to agglomerate due to their high aspect ratios and intrinsic van der Waals attraction [70]. Ultrasonication was used to aid in the dispersion of the nanotubes when fabricating the composites. First a 1:10 ratio mixture of CNTs and ethanol was sonicated for 2 hours using an ultrasonic cleaner at 40 kHz and 700 W. The mixture was then added to the hardener and sonicated for another hour. Next the suspension was vacuumed until all ethanol had evaporated. The CNT/hardener mixture was then added to the resin and mixed with a combination of mechanical mixing and sonication. After a few minutes of mixing, the samples were degassed to prevent gas bubbles from forming. The samples were then cured for 24 hours at room temperature. The nanocomposites contained 2.0 wt% CNTs. Samples were cut to thicknesses of 120, 240, and 360 µm using a slow speed diamond saw. The fracture surface of a MWCNT/epoxy composite sample is given in Figure 10.

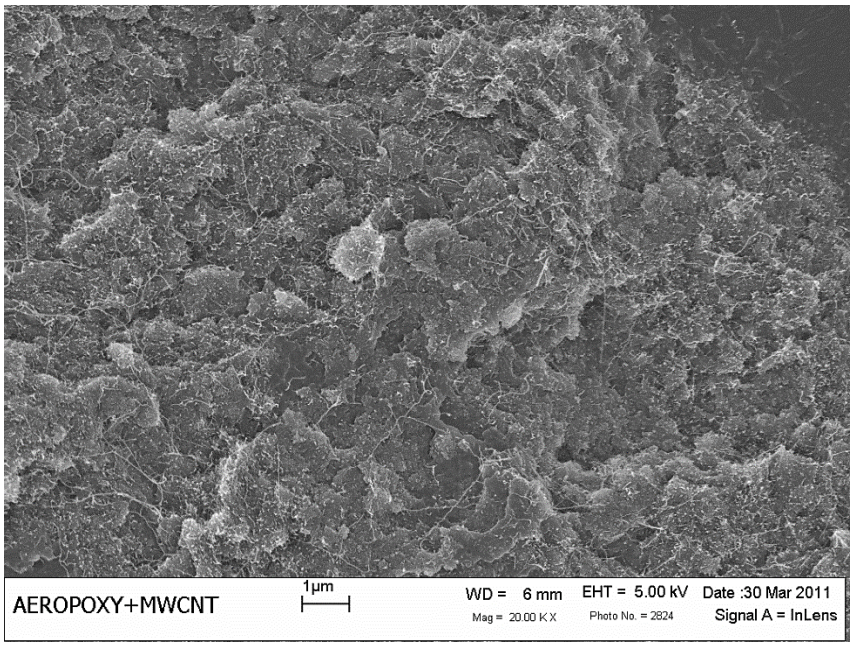

Figure 10: SEM micrograph of the fracture surface of a MWCNTs-Aeropoxy composite.

2.3 Proton Radiation Experiments

The Florida State University tandem Van de Graaff accelerator was used to provide energetic beams of protons. The tandem Van de Graaff accelerator can be used as a stand-alone accelerator or it can utilize a superconducting linear accelerator that can boost the beam energy further. The accelerators are capable of producing proton beams for experiments with continuously variable energies from 2-20 MeV and beams of all other nuclear species up to mass 40 except for the noble gases Ne and Ar with energies up to 6 MeV per amu for the beams over mass 28 and up to 8 MeV per amu for lighter beams.

The experimental setup for the energy loss measurement is shown in Figure 11. Collimating slits and apertures were used to limit the size and the angular divergence of the incident beam. The direct beam from the accelerator is much more intense than desired for the work here. Consequently the direct beam struck a thin gold foil and the scattered protons from this foil irradiated the samples of interest.

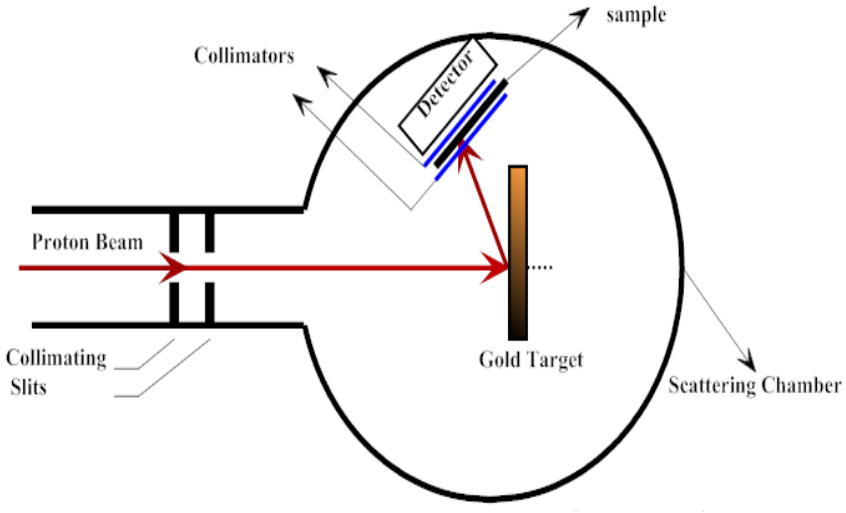

Figure 11: Schematic of experimental setup for irradiation and energy loss measurement [62]. Image used under fair use

The experiment was conducted in a vacuum scattering chamber. The scattered protons were detected with a Si surface barrier detector that was calibrated so that the proton energy could be read out directly. The energy loss of protons passing through the sample was found by determining the energy difference between protons with and without the sample being placed in front of the detector. Each sample was exposed to four different initial beam energies of 6.0, 8.0, 10.0, and 12.0 MeV for 10 minutes at each energy level. The beam exposure was cumulative, meaning that each sample was exposed all four beam energies, for a total exposure time of 40 minutes. As an alternative to measuring the beam's fluence, the beam current was measured to be approximately 1.50 nA. A sample measurement of the 240 μm thick epoxy film is shown in Figure 12.

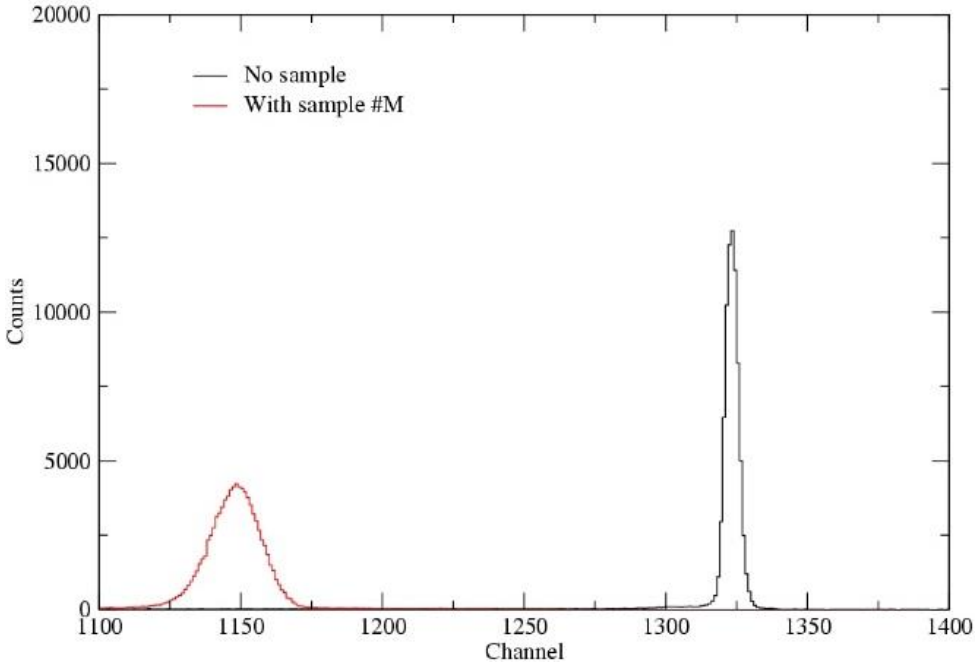

Figure 12: Proton counts with and without a 240 μm thick epoxy film

2.4 Nanoindentation

Nanoindentation is a technique for measuring the mechanical properties of small samples or examining surface effects. It is, in principle, identical to traditional micro-scale indentation tests but the load is on the mN scale and the indentation depth ranges between hundreds of nm and several microns while the projected indentation area is on the μm^2 scale. There are many different shapes and sizes of indenters, but they are all made from a very hard material such as diamond or tungsten. Figure 13 shows some of the common nanoindenter tip options. A 5.0 µm spherical tip was used for most of the samples but for the samples with considerable surface roughness a 50 µm spherical tip, which is one of the largest tips used for nanoindentation, was used because it is less susceptible to errors caused by surface roughness.

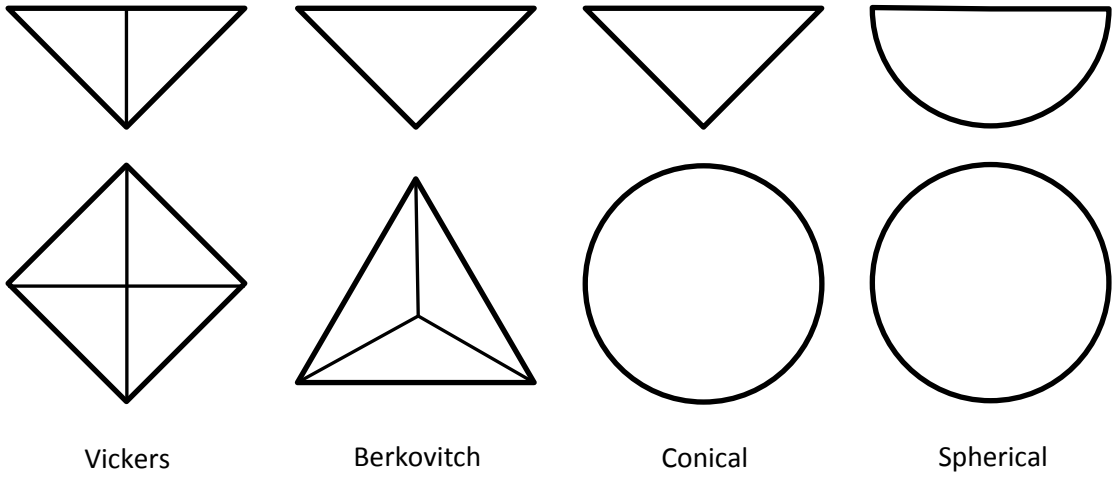

Figure 13: Schematic of indenter tips.

A NanoTest 600 nanoindentation system was used to perform the mechanical tests on our samples. Figure 14 shows a schematic representation of the system.

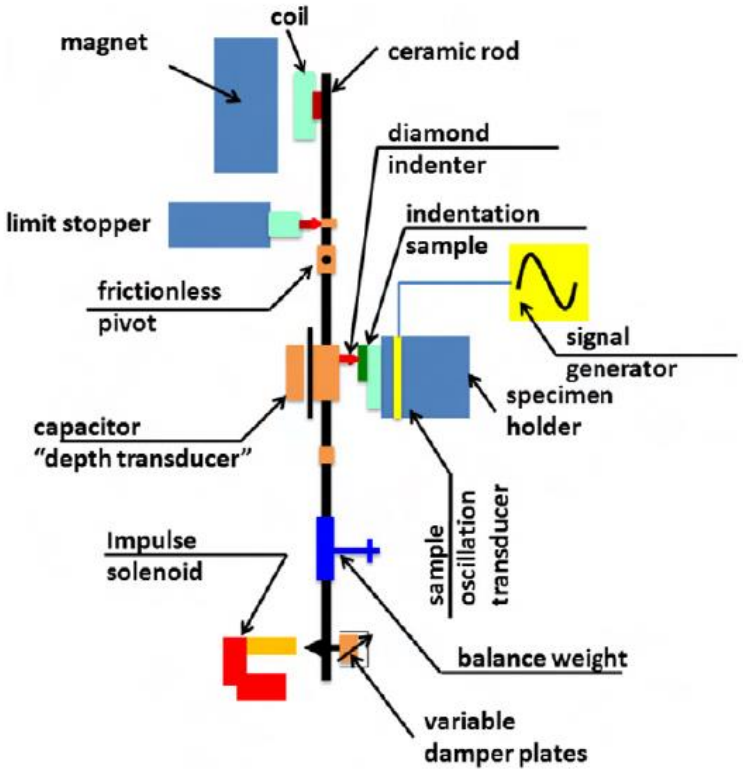

Figure 14: Schematic of NanoTest 600 system[62]. Image used under fair use

A typical nanoindentation experiment begins by loading the specimen to a specific load (usually in the range of μN to mN), then keeping the load constant to realize material creep (if needed), and finally unloading the specimen, leaving an indentation impression. This loading is performed by sending an electrical signal to the coil which causes the pendulum to rotate about its frictionless pivot so that the indenter penetrates the sample surface. The indenter tip displacement (penetration) is measured during loading and unloading with a parallel plate capacitor that has sub nanometer theoretical resolution.

A schematic representation of the loading and unloading process and the parameters used in analysis are shown in Figure 15 (a). The geometry of the indentation impression surface at

loading and unloading using the Berkovich pyramid indenter are shown in Figure 15 (b). The nanoindentation data was corrected for frame compliance and thermal drift. The analysis of the load-indentation depth was performed using the Oliver-Pharr method [71].

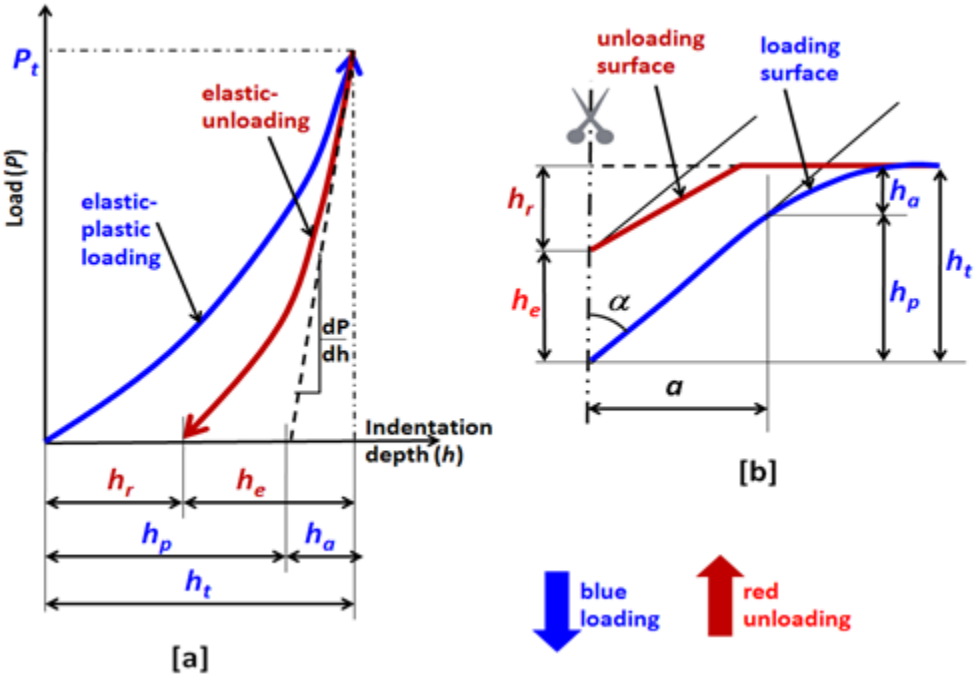

Figure 15: (a) Loading and unloading in nanoindentation and (b) schematic of the corresponding indenter/sample contact surface movement during loading and unloading [72]. Image used under fair use

We identify indentation depths: h_t, h_e, h_r as being total depth at load P_t, elastic depth rebound at unloading, and residual impression depth, respectively. We also define h_a as the displacement of the surface at the perimeter and h_p the contact indentation depth. Following these definitions one can conclude that

$$h_t = h_a + h_p \tag{2}$$

The contact area of a perfect Berkovich indenter can be computed as a function of the contact indentation depth (h_p) as

$$A = 3\sqrt{3}h_p{}^2 \tan^2 65.3 = 24.5h_p{}^2 \tag{3}$$

Contact area measurements from indenting a fused silica reference sample at different depths showed that the area is given by

$$A = 6883h_p + 21.031h_p^2 \tag{4}$$

The hardness (H) can thus be computed at the maximum indentation load (P_t) as

$$H = \frac{P_t}{A} \tag{5}$$

By considering the unloading response, we can observe the reduced modulus of specimen denoted E_r (representing the combined stiffness of sample and the indenter) which can be directly related to the elastic modulus of the sample E_s using

$$\frac{1}{E_r} = \frac{1-\upsilon_c{}^2}{E_s} + \frac{1-\upsilon_i^2}{E_i} \tag{6}$$

Where E_i and ν_i are the elastic modulus and Poisson's ratio of the indenter materials (E_i =800 GPa; ν_i = 0.27 for diamond indenter) and ν_c is Poisson's ratio of the sample. It is important to note that E_r can be used to represent our sample stiffness due to the very high stiffness of the indenter compared with epoxy. E_r can be computed from the unloading curve after Oliver-Pharr [71, 73]

$$E_r = \frac{1}{2\beta}\frac{dP}{dh}\sqrt{\frac{\pi}{A}} \tag{7}$$

Where $\frac{dP}{dh}$ is the slope of the first 60% span of the unloading curves as shown in Figure 15 (a) and A is the area of the indentation impression from Equation 4. The coefficient β is reported to be equal to 1.0 for the spherical indenter [72].

While the loading portion of the nanoindentation curve represents both the elastic and plastic deformations, the unloading portion represents the elastic behavior mainly, and thus the unloading result is what is used to calculate the elastic modulus. It is well known that to improve the accuracy of results from nanoindentation experiments in polymeric materials an evolution of short creep behavior is required. Upon reaching the maximum indentation load and holding it constant for few seconds, further depth increase arises due to creep. This creep behavior influences the maximum depth and slope of the upper portion of the unloading curve, which is used for calculating the contact stiffness and modulus. Thus creep can influence the results if not properly accounted for [74]. The loading and unloading rates utilized for this test were 0.1 mN/s, the maximum load was 10 mN, and the creep dwell period was set to 60 s.

Sometimes during a nanoindentation test, the indenter will come in contact with an anomalous surface feature such as a void, ridge, or impurity. In this case, the curve will often look significantly different from other curves generated by the same sample, and it will give an erroneous result. These results can be easily spotted by looking at the load-depth indentation curves. For each sample in this study, 15 indentations were performed and any clearly erroneous curves were removed before analysis. Figure 16 shows sample curves before (left) and after (right) removing erroneous curves.

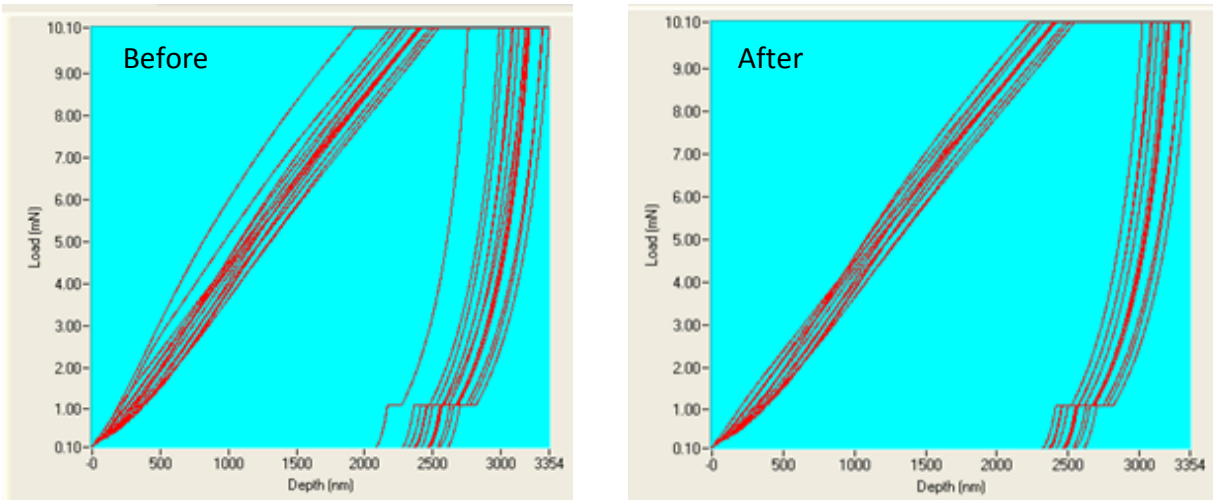

Figure 16: Indentation curves before and after removal of erroneous curves.

Figure 17 shows the indentation curves for the six 360 µm samples after removal of erroneous curves.

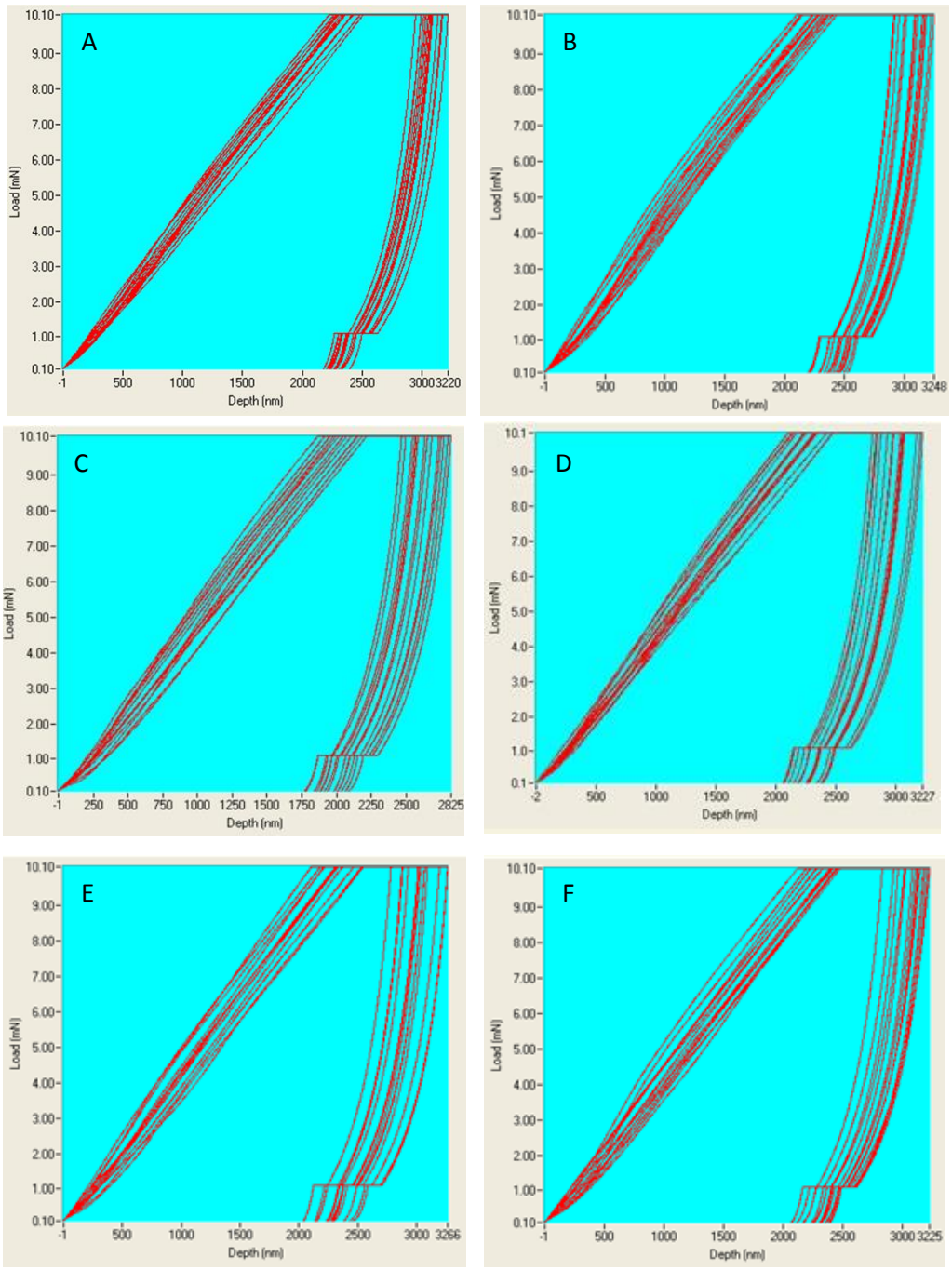

Figure 17: Sample nanoindentation curves. (A) N360 NR, (B) N360 Rad, (C) SW360 NR, (D) SW360 Rad, (E) MW360 NR, (F) MW360 Rad

2.5 Electrical Resistivity

The volume electrical resistivity of the different samples was measured using a Keithley model 6487 picoammeter/voltage source with a Keithley model 8009 resistivity test fixture capable of measuring volume resistivity as high as 10^{18}. Figure 18 shows a schematic of the test fixture.

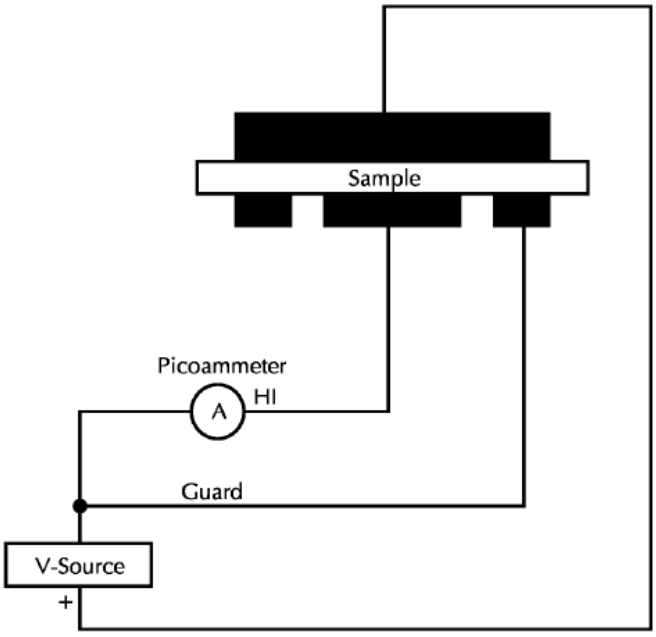

Figure 18: Schematic of resistivity measurement setup [75]. Image used under Fair Use.

The accepted method for measuring volume resistivity according to ASTM standard D257 [76] is to apply a voltage between 1 and 500 V for a set period of time (typically one minute is sufficient) and measure the resulting current. Knowing the voltage, V, the current, I, the area of the sample, A, and the thickness of the sample, t, the volume resistivity, ρ_v, can be calculated according to Equation 8.

$$\rho_v = \frac{AV}{tI} \tag{8}$$

However, for high impedance materials, the resulting currents are very low and it is difficult to get accurate and repeatable measurements. An alternating voltage method [75] was employed to reduce errors from background currents and drifts. In this method a positive voltage is applied and the current measured after a specific period of time, then a negative voltage of the same magnitude is immediately applied and the resulting current measured after waiting the same period of time. This process is repeated several times until four current measurements have been collected. The current, I_{calc}, superimposed on the background current in response to the stimulus voltage is calculated according to Equation 9.

$$I_{calc} = (I_1 - 3I_2 + 3I_3 - I_4)/8 \quad (9)$$

I_1 and I_3 are the positive polarity measurements and I_2 and I_4 are the negative polarity measurements. The composites containing nanotubes were subjected to an alternating positive and negative voltage of magnitude 1.0 V. Because the resistivity of the neat samples was so much higher than that of the composite samples, a higher voltage was needed in order to generate a measureable current. For the neat samples, a voltage of magnitude 500V was used.

2.6 Scanning Electron Microscopy (SEM)

The microstructures of the samples were examined using a Zeiss Field Emission Scanning Electron Microscope. The sample surfaces were coated with a thin layer of gold to prevent charging. Note that all the transport and mechanical tests were conducted prior to the microscopy to avoid any interference of the sputtered gold film.

Chapter 3: Results and Discussion

3.1 Proton Stopping Power

Table 2 shows the stopping power of each sample.

Table 2: Proton stopping power

	Energy Loss, MeV/mm				
Beam Energy	**6 MeV**	**8MeV**	**10 MeV**	**12 MeV**	**Average**
N120	7.53	5.97	5.01	4.41	5.73
MW120	7.02	5.74	4.79	4.09	5.41
SW120	7.70	6.06	4.86	4.43	5.77
N240	9.77	7.50	6.24	5.07	7.15
MW240	9.79	7.22	5.79	5.04	6.96
SW240	9.69	6.81	5.57	4.80	6.72
N360	10.15	7.12	5.97	4.75	7.00
MW360	11.25	7.46	6.03	4.96	7.43
SW360	10.49	7.07	5.72	4.82	7.02

In general, regardless of the material, as the thickness increases the stopping power increases since protons are traveling along a longer path and thus losing more of their energy. Also as the damage was accumulative (the same sample was exposed to 6MeV, 8MeV, 10 MeV, and 12 MeV sequentially) the shielding effectiveness degrades as the sample itself structurally degrades. There is no clear trend in stopping power between the neat, SWCNT, and MWCNT samples, indicating that the inclusion of nanotubes has no measurable effect on the stopping power at these energy levels. This data can be visualized in Figure 19.

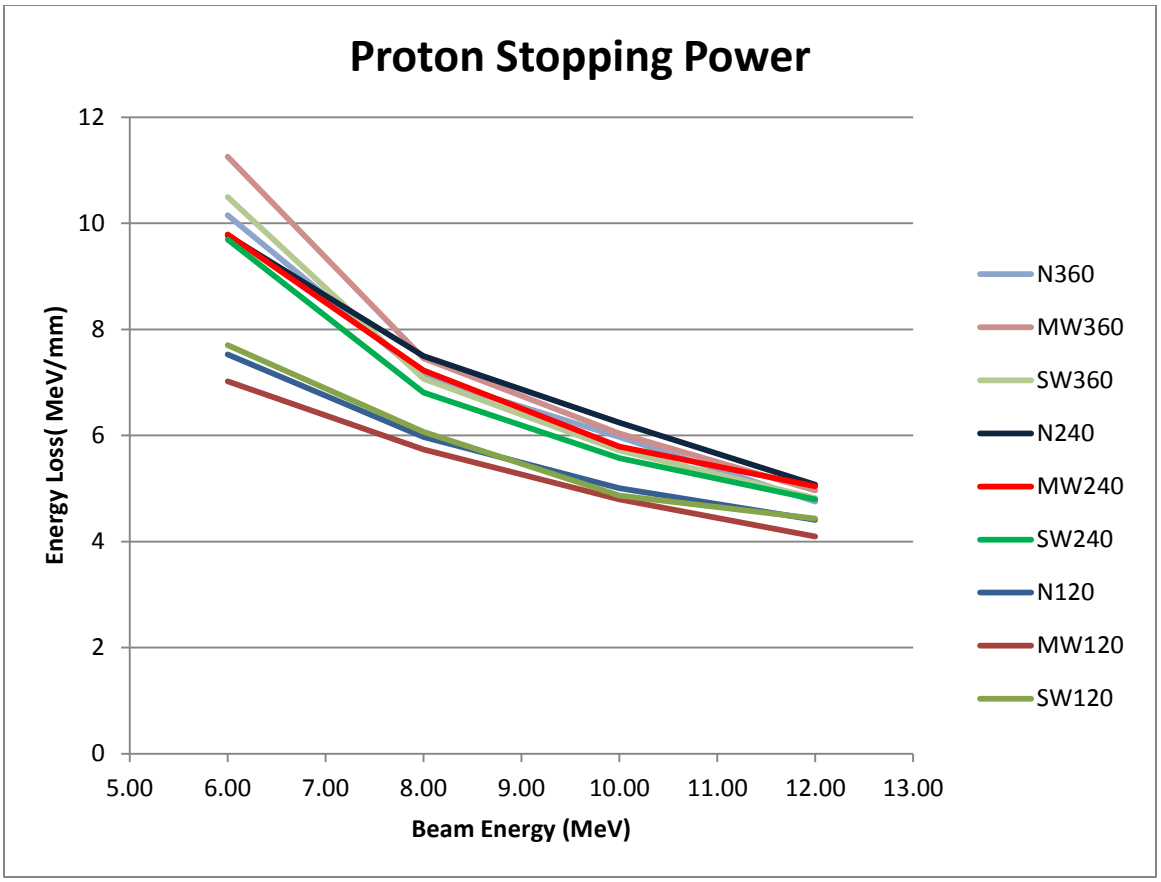

Figure 19: Stopping power

3.2 Nanoindentation

The mechanical properties of all the samples were first measured with a Berkovitch tip, but the effect of surface roughness was far too strong for the data to be meaningful, as indicated by coefficient of variations (CVs) in the range of 15%-30%. Due to the surface roughness of the samples, a 5 µm diameter spherical indenter was used. As a result, the effect of surface roughness was reduced, but it still dominated any radiation induced changes as shown in Table 3 and Table 4.

Table 3: Effect of radiation on elastic modulus

	NonRadiated		Radiated		Effect of Radiation	
	Modulus (GPa)		Modulus (GPa)		Modulus (GPa)	
	Mean	CV	Mean	CV	% Change	Combined CV
N120	4.06	7.67	3.88	7.25	-4.42	14.92
N240	4.52	6.22	4.63	4.46	2.36	10.69
N360	4.71	5.46	4.96	3.24	5.35	8.70
SW120	4.08	5.84	3.97	5.76	-2.48	11.60
SW240	4.80	2.61	4.77	3.35	-0.68	5.96
SW360	4.43	4.65	4.45	3.73	0.64	8.38
MW120	3.83	4.95	3.99	5.06	4.05	10.02
MW240	4.54	4.27	4.61	3.96	1.55	8.23
MW360	4.42	4.77	4.25	5.46	-3.72	10.22

Table 4: Effect of radiation on hardness

	NonRadiated		Radiated		Effect of Radiation	
	Hardness (GPa)		Hardness (GPa)		Hardness (GPa)	
	Mean	CV	Mean	CV	% Change	Combined CV
N120	0.215	*2.561*	0.214	*1.606*	-0.430	*4.167*
N240	0.213	*1.235*	0.215	*1.287*	1.123	*2.522*
N360	0.219	*1.969*	0.218	*1.597*	-0.425	*3.566*
SW120	0.230	*2.350*	0.230	*2.109*	-0.216	*4.459*
SW240	0.229	*2.406*	0.230	*3.165*	0.332	*5.571*
SW360	0.220	*2.397*	0.222	*2.112*	0.591	*4.509*
MW120	0.218	*2.198*	0.216	*0.003*	-1.099	*2.200*
MW240	0.227	*3.303*	0.222	*0.006*	-2.013	*3.309*
MW360	0.221	*2.115*	0.219	*0.004*	-0.974	*2.119*

Notice that none of the changes in modulus are greater than the combined coefficient of variation of the two measurements used to calculate that difference. Because these samples were cut with a saw, the surface roughness is too great to make accurate measurements with the nanoindenter.

After examining the samples under SEM, it was evident that the 240 µm samples had a higher surface roughness than the other samples, so the tests were performed again on the 240 µm samples using a 50 µm spherical tip to minimize the errors associated with the surface roughness. The 50 µm tip did not significantly improve the results, as can be seen in Table 5.

Table 5: Effect of radiation on 240 µm samples using a 50 µm spherical tip

	Nonradiated		Irradiated		Effect of Radiation	
	Modulus (GPa)		Modulus (GPa)		Modulus (GPa)	
	Mean	CV	Mean	CV	% Change	Combined CV
N240	3.26	*2.48*	2.36	*4.50*	-27.65	*6.98*
SW240	2.68	*7.40*	2.99	*4.14*	11.43	*11.54*
MW240	2.32	*3.86*	2.30	*6.27*	-0.66	*10.12*

The changes in elastic modulus of the non-radiated samples as a result of addition of CNTs are summarized in Table 6.

Table 6: Effect of CNTs on modulus

	Modulus (GPa)			
	Mean	CV	% Change	Combined CV
N120	4.06	*7.67*	NA	NA
N240	4.52	*6.22*	NA	NA
N360	4.71	*5.46*	NA	NA
SW120	4.08	*5.84*	0.31	*13.51*
SW240	4.80	*2.61*	6.17	*8.83*
SW360	4.43	*4.65*	-6.04	*10.11*
MW120	3.83	*4.95*	-5.65	*12.62*
MW240	4.54	*4.27*	0.45	*10.49*
MW360	4.42	*4.77*	-6.24	*10.22*

Note that none of the changes in modulus are larger than the coefficient of variations.

Table 7 shows the changes in the hardness of the neat samples after addition of CNTs.

Table 7: Effect of CNTs on hardness

	Hardness (GPa)			
	Mean	**CV**	**% Change**	**Combined CV**
N120	0.215	*2.561*	NA	NA
N240	0.213	*1.235*	NA	NA
N360	0.219	*1.969*	NA	NA
SW120	0.230	*2.350*	7.22	*4.91*
SW240	0.229	*2.406*	7.69	*3.64*
SW360	0.220	*2.397*	0.67	*4.37*
MW120	0.218	*2.198*	1.44	*4.76*
MW240	0.227	*3.303*	6.71	*4.54*
MW360	0.221	*2.115*	1.14	*4.08*

The hardness of each sample increased with the addition of CNTs, with many of the changes being greater than a coefficient of variation. We would expect the hardness of the samples to increase with addition of CNTs, since CNTs are harder and stronger than the epoxy matrix, and the results follow our expectations.

While it was possible to conclude that addiction of the CNTs increased the hardness of the samples, the high level of surface roughness made more precise measurement of the mechanical properties impossible.

3.3 Electrical Resistivity

The resistivity of the composite samples containing nanotubes was found to be about 5 orders of magnitude lower than that of the neat samples. Irradiation reduced the resistivity of all the samples but to somewhat different degrees as shown in Figure 20. Clearly there is a lot of scatter in the data, but a trend can still be seen.

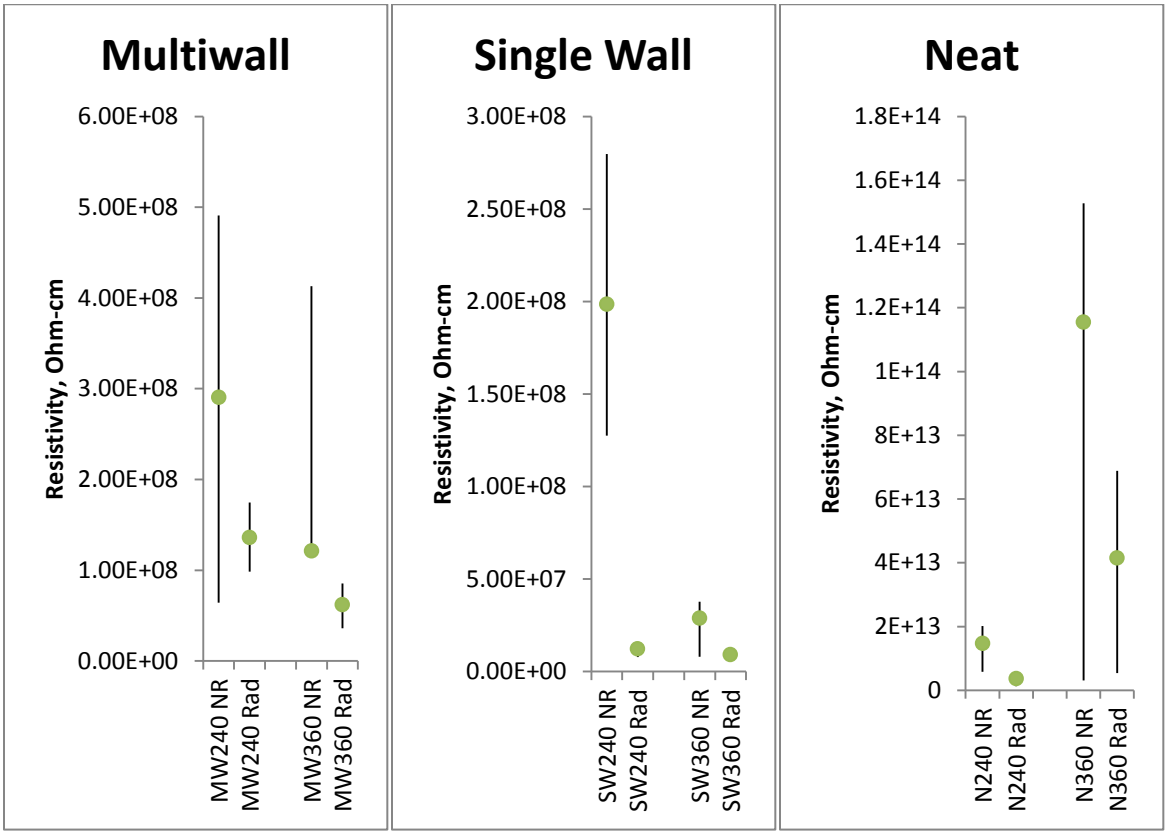

Figure 20: Average resistivity (circle), and range from 1st to 3rd quartile (line)

Table 8 shows a summary of the resistivity data. The SWCNT based composites showed the greatest reduction in resistivity due to irradiation, with a reduction of about an order of magnitude. The MWCNT based composite and the neat samples both also saw a significant reduction in resistivity after being irradiated.

Table 8: Summary of electrical resistivity data

	Average (Ω.cm)		
MWCNTs	**NR**	**Rad**	**Ratio NR/Rad**
360 μm	1.21E+08	6.19E+07	1.96
240μm	2.90E+08	1.36E+08	2.14
Average	2.06E+08	9.89E+07	2.05
	Average (Ω.cm)		
SWCNTs	**NR**	**Rad**	**Ratio NR/Rad**
360μm	2.87E+07	9.11E+06	3.15
240 μm	1.99E+08	1.23E+07	16.17
Average	1.14E+08	1.07E+07	9.66
	Average (Ω.cm)		
Neat	**NR**	**Rad**	**Ratio NR/Rad**
360 μm	1.15E+14	4.15E+13	2.78
240 μm	1.47E+13	3.68E+12	4.00
Average	6.51E+13	2.26E+13	3.39

3.4 Scanning Electron Microscopy

The dominant feature apparent from SEM imaging was surface roughness as shown in Figure 21. There is no obvious visual damage caused by radiation that can be seen under SEM. EDS confirmed that no gold particles had been deposited on the surface during irradiation.

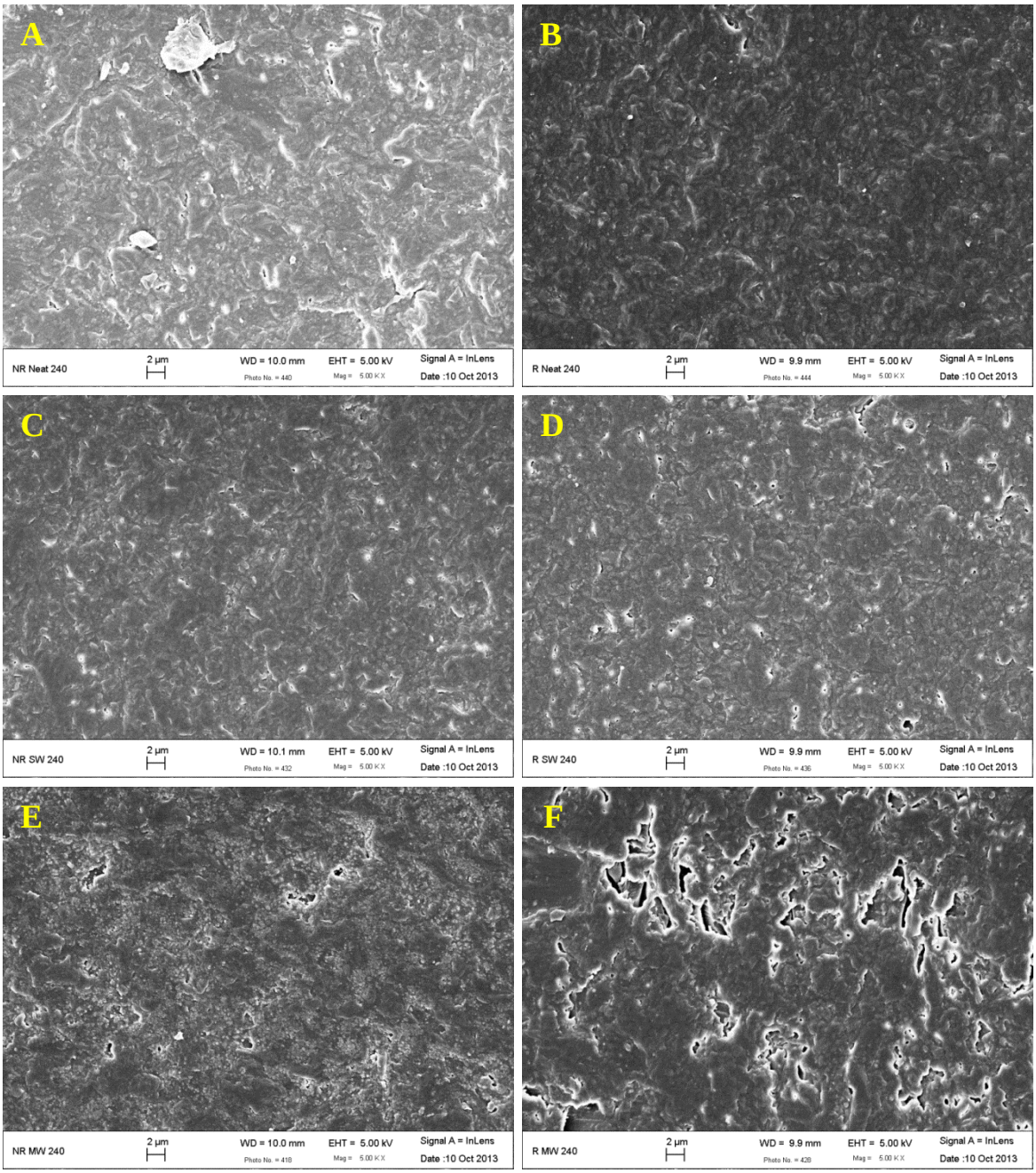

Figure 21: SEM images of 240 µm samples. A is nonradiated neat, B is radiated neat, C is nonradiated single wall, D is radiated single wall, E is nonradiated multiwall, and F is radiated multiwall.

Chapter 4: Conclusions and Recommendations

It was found that the stopping power of an epoxy sample was not affected by the addition of CNTs. A significant change in the stopping power was not expected because there is only 2 wt% CNTs in each composite and the stopping power of carbon is only slightly lower than that of the epoxy. This is a promising result for cosmic radiation shielding as the addiction of CNTs was shown to improve the mechanical and electrical properties of the samples.

As can be seen in the electron micrographs of the samples, the surface roughness is very high. The roughness of the samples most likely played a significant role in the inability to make precise measurements with the nanoindenter. It is recommended that future work on this subject attempt to minimize surface roughness. The surface roughness of the samples was caused by cutting them to size with a saw. Some alternative fabrication methods that may reduce surface roughness include slicing the samples, spin coating them, and molding them to the desired size. Another approach to minimizing the effects of surface roughness is to fabricate thicker samples so that the penetration depth of the nanoindentation tests can be increased. As the penetration depth of the test increases, surface effects are minimized.

The addition of CNTs decreased the electrical resistivity of the samples by around five orders of magnitude. A reduction in the resistivity was expected since CNTs are much more conductive than polymers, and with good dispersion, they should provide conductive paths through the insulating epoxy. Decreases in electrical conductivity when CNTs are added to polymers have been well documented in the literature. In fact, it is one of the major methods of quantifying CNT dispersion since conductivity generally increases with better CNT dispersion.

Proton irradiation reduced the resistivity of the samples by a factor of around 2-16. Because the resistivity is dominated by the regions between CNTs where the charge carriers must traverse the insulating epoxy, changes to the resistivity of the epoxy have a stronger influence on the resistivity of the composite than changes to the resistivity of the CNTs. It is believed that the primary cause of the increase in conductivity of the polymer matrix is the increase in conjugated double bonds which promote the motion of charge carriers along the polymeric chains. This hypothesis can be tested in future work by comparing the infrared and UV-VIS spectra of the radiated and non-radiated samples. Radiation has also been shown to change the electrical conductivity of CNTs, but this effect is likely to be negligible.

As protons are not the only source of cosmic radiation, it would be useful to examine the effects of other types of radiation on these composites as well. The strong relation between irradiation and resistivity could be exploited to create a new type of radiation sensor. For this to be explored, much more detailed analysis of resistivity dose dependence is needed. It would be valuable to expose several identical samples to different fluences and energies of irradiation to develop a comprehensive understanding of the effects. It is also recommended that micro-Raman analysis be undertaken to identify the specific changes to the microstructure that are occurring.

References

1. Cucinotta, F.A. and M. Durante, *Cancer risk from exposure to galactic cosmic rays: implications for space exploration by human beings.* The lancet oncology, 2006. **7**(5): p. 431-435.
2. Fry, R.J.M., et al., *Guidance on radiation received in space activities*, 1989, National Council on Radiation Protection and Measurements: Bethesda, MD.
3. Benton, E. and E. Benton, *Space radiation dosimetry in low-Earth orbit and beyond.* Nuclear Instruments and Methods in Physics Research Section B: Beam Interactions with Materials and Atoms, 2001. **184**(1): p. 255-294.
4. Ackermann, M., et al., *Detection of the characteristic pion-decay signature in supernova remnants.* Science, 2013. **339**(6121): p. 807-811.
5. Stauber, M., M. Rossi, and E. Stassinopoulos, *An overview of radiation hazards in Earth orbits*, in *Space Safety and Rescue*, G.W. Heath, Editor 1983, American Astronautical Society, Univelt Inc.: San Diego, California. p. 267.
6. Smart, D. and M. Shea, *Solar proton events during the past three solar cycles.* Journal of Spacecraft and Rockets, 1989. **26**(6): p. 403-415.
7. Simpson, J., *Elemental and isotopic composition of the galactic cosmic rays.* Annual Review of Nuclear and Particle Science, 1983. **33**(1): p. 323-382.
8. Letaw, J., R. Silberberg, and C. Tsao, *Radiation hazards on space missions outside the magnetosphere.* Advances in Space Research, 1989. **9**(10): p. 285-291.
9. King, J.H., *Solar proton fluences for 1977-1983 space missions.* Journal of Spacecraft and Rockets, 1974. **11**(6): p. 401-408.
10. Barghouty, A.F. and S.A. Thibeault, *The exploration atmospheres working group's report on space radiation shielding materials*, 2006, NASA: Marshall Space Flight Center, Alabama.
11. Stassinopoulos, E.G., *SOLPRO: a computer code to calculate probabilistic energetic solar proton fluences*, 1975, NASA: Goddard Space Flight Center, Greenbelt, Maryland, USA.
12. Burrell, M.O., *The risk of solar proton events to space missions*, in *National Symposium on Natural and Manmade Radiation in Space,* 1972, NASA: Marshall Space Flight Center; Huntsville, AL, United States. p. 310-323.
13. Booyabazooka, *File:Van Allen radiation belt.svg*, 2006, Wikimedia Commons.
14. Curtis, S., et al., *Radiation environments and absorbed dose estimations on manned space missions.* Advances in Space Research, 1986. **6**(11): p. 269-274.
15. IAEA, *Relative biological effectiveness in ion beam therapy.* Technical Reports Series no. 461, 2008.
16. Wilson, J., et al., *Issues in deep space radiation protection.* Acta Astronautica, 2001. **49**(3): p. 289-312.
17. Miller, J., et al., *Ground-based simulations of cosmic ray heavy ion interactions in spacecraft and planetary habitat shielding materials.* Acta Astronautica, 1998. **42**(1): p. 389-394.
18. Spillantini, P., et al., *Shielding from cosmic radiation for interplanetary missions: active and passive methods.* Radiation Measurements, 2007. **42**(1): p. 14-23.
19. Wilson, J.W., et al. *Shielding strategies for human space exploration*. in *Workshop on Shielding Strategies for Human Space Exploration*. 1997. Houston, Texas: NASA.
20. Wilson, J.W., et al., *Transport methods and interactions for space radiations*, in *Biological Effects and Physics of Solar and Galactic Cosmic Radiation*, C.E. Swenberg, G. Horneck, and E.G. Stassinopoulos, Editors. 1991, Plenum Press: New York. p. 187-786.
21. Kaul, R., A. Barghouty, and H. Dahche, *Space radiation transport properties of polyethylene-based composites.* Annals of the New York Academy of Sciences, 2004. **1027**(1): p. 138-149.

22. Koelle, D., *Specific transportation costs to GEO—past, present and future.* Acta Astronautica, 2003. **53**(4): p. 797-803.
23. Adams Jr., J.H., et al., *Revolutionary concepts of radiation shielding for human exploration of space.* NASA, 2005. **213688**: p. 1-108.
24. Shultis, J. and R. Faw, *Fundamentals of Nuclear Science and Engineering*. 2002, New York: Marcel Dekker, Inc.
25. Wilson, J.W., et al., *Issues in space radiation protection: galactic cosmic rays.* Health Physics, 1995. **68**(1): p. 50-58.
26. Simonsen, L.C. and J.E. Nealy, *Radiation protection for human missions to the Moon and Mars.* NASA Technical Paper, 1991. **3079**: p. 1-30.
27. Chen, P., et al., *High H2 uptake by alkali-doped carbon nanotubes under ambient pressure and moderate temperatures.* Science, 1999. **285**(5424): p. 91-93.
28. Chambers, A., et al., *Hydrogen storage in graphite nanofibers.* The Journal of Physical Chemistry B, 1998. **102**(22): p. 4253-4256.
29. Liu, C., et al., *Hydrogen storage in single-walled carbon nanotubes at room temperature.* Science, 1999. **286**(5442): p. 1127-1129.
30. Dillon, A.C., et al., *Storage of hydrogen in single-walled carbon nanotubes.* Nature, 1997. **386**(6623): p. 377-379.
31. Stratton, J., R. Harvey, and G. Heyler, *Mission Overview for the Radiation Belt Storm Probes Mission.* Space Science Reviews, 2013. **179**(1-4): p. 29-57.
32. Iijima, S., *Helical microtubules of graphitic carbon.* Nature, 1991. **354**: p. 56-58.
33. Wang, X., et al., *Fabrication of ultralong and electrically uniform single-walled carbon nanotubes on clean substrates.* Nano Letters, 2009. **9**(9): p. 3137-3141.
34. Thostenson, E.T., Z. Ren, and T.-W. Chou, *Advances in the science and technology of carbon nanotubes and their composites: a review.* Composites Science and Technology, 2001. **61**(13): p. 1899-1912.
35. Treacy, M.M.J., T.W. Ebbesen, and J.M. Gibson, *Exceptionally high Young's modulus observed for individual carbon nanotubes.* Nature, 1996. **381**(6584): p. 678-680.
36. Poncharal, P., et al., *Electrostatic deflections and electromechanical resonances of carbon nanotubes.* Science, 1999. **283**(5407): p. 1513-1516.
37. Krishnan, A., et al., *Young's modulus of single-walled nanotubes.* Physical Review B, 1998. **58**(20): p. 14013-14019.
38. Wong, E.W., P.E. Sheehan, and C.M. Lieber, *Nanobeam mechanics: elasticity, strength, and toughness of nanorods and nanotubes.* Science, 1997. **277**(5334): p. 1971-1975.
39. Salvetat, J.-P., et al., *Elastic and shear moduli of single-walled carbon nanotube ropes.* Physical Review Letters, 1999. **82**(5): p. 944-947.
40. Yu, M.-F., et al., *Strength and breaking mechanism of multiwalled carbon nanotubes under tensile load.* Science, 2000. **287**(5453): p. 637-640.
41. Dresselhaus, M.S., et al., *Carbon Nanotubes*, in *The Physics of Fullerene-Based and Fullerene-Related Materials*, W. Andreoni, Editor. 2000, Springer Netherlands: Dordrecht, The Netherlands. p. 331-379.
42. Falvo, M., et al., *Bending and buckling of carbon nanotubes under large strain.* Nature, 1997. **389**(6651): p. 582-584.
43. Wagner, H., et al., *Stress-induced fragmentation of multiwall carbon nanotubes in a polymer matrix.* Applied Physics Letters, 1998. **72**(2): p. 188-190.
44. Walters, D., et al., *Elastic strain of freely suspended single-wall carbon nanotube ropes.* Applied Physics Letters, 1999. **74**(25): p. 3803-3805.

45. Demczyk, B., et al., *Direct mechanical measurement of the tensile strength and elastic modulus of multiwalled carbon nanotubes.* Materials Science and Engineering: A, 2002. **334**(1): p. 173-178.
46. Muster, J., et al., *Scanning force microscopy characterization of individual carbon nanotubes on electrode arrays.* Journal of Vacuum Science & Technology B: Microelectronics and Nanometer Structures, 1998. **16**(5): p. 2796-2801.
47. Baughman, R.H., A.A. Zakhidov, and W.A. de Heer, *Carbon nanotubes--the route toward applications.* Science, 2002. **297**(5582): p. 787-792.
48. Lu, X. and Z. Chen, *Curved pi-conjugation, aromaticity, and the related chemistry of small fullerenes.* Chemical Reviews, 2005. **105**(10): p. 3643-3696.
49. Soh, H.T., et al., *Integrated nanotube circuits: controlled growth and ohmic contacting of single-walled carbon nanotubes.* Applied Physics Letters, 1999. **75**(5): p. 627-629.
50. Collins, P.G. and P. Avouris, *Nanotubes for electronics.* Scientific American, 2000. **283**(6): p. 62-69.
51. Crespi, V.H., et al., *Anisotropic electron-beam damage and the collapse of carbon nanotubes.* Physical Review B, 1996. **54**(8): p. 5927-5931.
52. Beuneu, F., et al., *Modification of multiwall carbon nanotubes by electron irradiation: an ESR study.* Physical Review B, 1999. **59**(8): p. 5945-5949.
53. Terrones, M., et al., *Coalescence of single-walled carbon nanotubes.* Science, 2000. **288**(5469): p. 1226-1229.
54. Krasheninnikov, A., et al., *Ion-irradiation-induced welding of carbon nanotubes.* Physical Review B, 2002. **66**(245403): p. 1-6.
55. Krasheninnikov, A., K. Nordlund, and J. Keinonen, *Production of defects in supported carbon nanotubes under ion irradiation.* Physical Review B, 2002. **65**(165423): p. 1-8.
56. Pomoell, J., et al., *Stopping of energetic ions in carbon nanotubes.* Nuclear Instruments and Methods in Physics Research Section B: Beam Interactions with Materials and Atoms, 2003. **206**: p. 18-21.
57. Wei, B., et al., *Tailoring structure and electrical properties of carbon nanotubes using kilo-electron-volt ions.* Applied Physics Letters, 2003. **83**(17): p. 3581-3583.
58. Ishaq, A., et al., *Graphite-to-amorphous structural transformation of multiwalled carbon nanotubes under proton beam irradiation.* Materials Letters, 2009. **63**(17): p. 1505-1507.
59. Neupane, P.P., et al., *Proton irradiation effect on single-wall carbon nanotubes in a poly (3-octylthiophene) matrix.* Applied Physics Letters, 2005. **86**(221908).
60. Kyriakou, I., et al., *Energy loss of protons in carbon nanotubes: experiments and calculations.* Nuclear Instruments and Methods in Physics Research Section B: Beam Interactions with Materials and Atoms, 2010. **268**(11): p. 1781-1785.
61. Chapiro, A., *Radiation chemistry of polymers*, in *Basic Mechanisms in the Radiation Chemistry of Aqueous Media,* 1964, Radiation Research Society: Gatlinburg, Tennessee. p. 179-191.
62. Al-Haik, M., et al., *Nanocharacterization of proton radiation damage on magnetically oriented epoxy.* International Journal of Polymer Analysis and Characterization, 2007. **12**(6): p. 413-430.
63. Kudoh, H., et al., *High energy ion irradiation effects on polymer materials: 2. Proton irradiation effects on PMMA and GFRP.* Polymer, 1996. **37**(21): p. 4663-4665.
64. Mishra, R., et al., *Optical and electrical properties of some electron and proton irradiated polymers.* Nuclear Instruments and Methods in Physics Research Section B: Beam Interactions with Materials and Atoms, 2000. **168**(1): p. 59-64.
65. Calcagno, L., G. Compagnini, and G. Foti, *Structural modification of polymer films by ion irradiation.* Nuclear Instruments and Methods in Physics Research Section B: Beam Interactions with Materials and Atoms, 1992. **65**(1): p. 413-422.

66. Little, K., *Irradiation of linear high polymers.* Nature, 1952. **170**(4338): p. 1075-1076.
67. Sasuga, T., et al., *Effects of ion irradiation on the mechanical properties of several polymers.* International Journal of Radiation Applications and Instrumentation. Part C. Radiation Physics and Chemistry, 1991. **37**(1): p. 135-140.
68. Parada, M., et al., *Effects of MeV proton bombardment in thin film PFA and FEP polymers.* Surface and Coatings Technology, 2005. **196**(1): p. 378-382.
69. Gao, Y., et al., *A study on radiation effect of < 200keV protons on M40J/epoxy composites.* Nuclear Instruments and Methods in Physics Research Section B: Beam Interactions with Materials and Atoms, 2005. **229**(2): p. 261-268.
70. Tehrani, M., M. Safdari, and M.S. Al-Haik, *Nanocharacterization of creep behavior of multiwall carbon nanotubes/epoxy nanocomposite.* International Journal of Plasticity, 2011. **27**(6): p. 887-901.
71. Oliver, W.C. and G.M. Pharr, *Improved technique for determining hardness and elastic modulus using load and displacement sensing indentation experiments.* Journal of Materials Research, 1992. **7**(6): p. 1564-1583.
72. Fischer-Cripps, A.C., *Nanoindentation*. 3 ed. 2011, New York: Springer.
73. Li, K., X.-L. Gao, and A. Roy, *Micromechanical modeling of viscoelastic properties of carbon nanotube-reinforced polymer composites.* Mechanics of Advanced Materials and Structures, 2006. **13**(4): p. 317-328.
74. Chudoba, T. and F. Richter, *Investigation of creep behaviour under load during indentation experiments and its influence on hardness and modulus results.* Surface and Coatings Technology, 2001. **148**(2): p. 191-198.
75. Daire, A., *Improving the repeatability of ultra-high resistance and resistivity measurements.* Keithley White Paper, 2004(1808).
76. ASTM, *Standard Test Methods for DC Resistance or Conductance of Insulating Materials*, in *ASTM Standard D,* 1993.